*fractal and fractional*

MDPI

*Article*

# Macroscopic Characterization and Microscopic Pore Structure of Permian Shale Reservoirs in Hunan–Guizhou–Guangxi Basin: Insights from NMRC, Fractal and Image-J Methods

**Yue Sun [1,2], Yuqiang Jiang [1,2,*], Miao Li [1,2], Xiangfeng Wei [3], Jingyu Hao [3] and Yifan Gu [1,2]**

[1] State Key Laboratory of Oil and Gas Reservoir Geology and Exploitation, Southwest Petroleum University, Chengdu 610500, China
[2] School of Geoscience and Technology, Southwest Petroleum University, Chengdu 610500, China
[3] Sinopec Exploration Company, Chengdu 610041, China
* Correspondence: xnsyjyq3055@126.com

## Abstract

Permian shale is the largest and most promising shale gas exploration target in southern China after Silurian shale. The fine evaluation of shale reservoirs is a prerequisite for large-scale exploration and development. Based on the fractal method, this study, through the combined technology of nuclear magnetic resonance cryoporometry (NMRC) and Image recognition software (Image-J), clarifies the pore size distribution of Permian shale in the HGG Basin. The purpose of this study is to characterize the macroscopic parameters of Permian shale and reveal the level of reservoir space development in Permian shale. The controlling factors of porosity and pore structure are demonstrated. It is suggested that Permian shales in the HGG Basin have organic carbon contents similar to marine shales. In the favorable interval of the Dalong Formation, the average organic carbon content is comparable to that of the LMX pay zone. The lower Longtan shales have the highest organic carbon and the greatest gas generation potential, followed by the Dalong shales. TOC is the primary control on porosity in the lower Longtan and Dalong formations, whereas clay minerals dominate the control in the upper Longtan. Abundant pores between grains and between layers within clay minerals account for most of the porosity in Upper Longtan shale. In the lower Longtan and Dalong formations, organic pores are pervasive, explaining the difference in the dominant controls on porosity between these intervals. Clay minerals are a key control on the development of Permian shale reservoirs. The fractal dimension of adsorption pores ($D_A$) has no clear relationship with the total clay content, is negatively correlated with the illite content, and shows no clear relationship with the chlorite content. In contrast, the fractal dimension of flow pores ($D_S$) shows a weak positive correlation with the total clay content, a clear positive correlation with the illite content, and a negative correlation with the chlorite content. When illite interacts with water, it tends to break down and plug pores, an effect that is especially pronounced in the smallest pores hosted by organic matter; this accounts for the negative correlation between $D_A$ and the illite content. In larger, flow-bearing pores, disintegrated illite roughens otherwise smooth walls between and within grains, increasing structural complexity and raising $D_S$. By contrast, reactions between chlorite and pore fluids tend to smooth the walls of flow pores, reducing structural complexity and lowering $D_S$.

**Keywords:** NMRC; Permian shale; controlling factor; Hunan–Guizhou–Guangxi Basin; fractal method

Check for updates

Academic Editor: Shengwen Tang

Received: 6 March 2026
Revised: 3 April 2026
Accepted: 5 April 2026
Published: 23 April 2026

**Copyright:** © 2026 by the authors. Licensee MDPI, Basel, Switzerland. This article is an open access article distributed under the terms and conditions of the Creative Commons Attribution (CC BY) license.

## 1. Introduction

Following the commercial success of shale gas and shale oil development in the United States and the commercial development of marine shale gas in the Sichuan Basin, hydrocarbons in shale have become a central focus for industry and academia. In response, the Ministry of Land and Resources of the People's Republic of China assessed the national shale resource potential and delineated five broad shale gas regions: the Northwest; the North and Northeast; the Upper Yangtze and Yunnan–Guizhou–Guangxi; the Middle–Lower Yangtze and Southeast; and the Qinghai–Tibet region. The assessment indicates that China has substantial shale gas potential, with a wide geographic distribution and multiple productive geologic intervals. Preliminary estimates indicate that Permian shale gas in China contains about 18.19 trillion cubic meters of resources, with approximately 2.67 trillion cubic meters considered recoverable. Among major stratigraphic units, the Permian System ranks third in shale gas potential, behind the Cambrian and Jurassic. Two distinct types of high-quality shale occur in the Hunan–Guizhou–Guangxi Basin (HGG Basin), and they meet the basic conditions for shale gas generation in marine and marine–terrestrial transitional depositional settings [1,2]. However, key attributes—including depositional setting, thickness, geochemical characteristics, hydrocarbon generation potential, mineral composition, and gas content—require further detailed study [3]. Building on this context, sedimentary evolution studies suggest that the region offers favorable geological conditions for shale gas [4]. Within the HGG Basin, the Permian Dalong and Longtan formations are widespread [5], occur at relatively shallow depths, are sufficiently thick, and contain shales that are rich in organic matter and mature enough to generate hydrocarbons [4]. The development of Permian shale gas resources exceeding one trillion cubic meters in recoverable reserves in Guangxi could significantly increase the proportion of clean energy in the regional energy mix, supporting the green transformation of the HGG Basin industrial belt. Results from exploratory wells, including S1 and XY1, further demonstrate the basin's exploration potential. In well XY1, the Permian Dalong–Longtan shale interval has gas contents of 0.16 $m^3/t$–1.41 $m^3/t$ and a tested production rate of $0.23 \times 10^4$ $m^3/d$ (~2300 $m^3/d$) [6]. As a clean energy source, it can replace coal to provide stable power for industrial hubs such as Liuzhou, thereby alleviating carbon emissions pressure from energy-intensive industries. Demonstration projects have cumulatively produced gas contents of over $1.13 \times 10^6$ $m^3$, validating the feasibility of localized energy supply. Consequently, through a threefold approach of energy substitution, feedstock conversion, and technological innovation, Permian shale gas in the Xiang–Gui Block is poised to become a core driver for advancing low-carbon industrial transition in South China, with projections indicating it could contribute over 30% of regional natural gas consumption by 2035.

Because the structural setting and the conditions that control how shale gas accumulates are complex, the HGG Basin likely differs from other regions in its accumulation mechanisms and distribution patterns. Building on earlier work, further study is needed to assess the exploration and development potential of Permian shales. Previous studies offer differing interpretations. Liu (2005) reported that, starting in the Middle Permian (Maokou Formation), the northern and southern parts of the HGG Basin developed distinct sedimentary environments as the basin evolved [7]. He linked this split to the interaction between basin development and nearby mountain building. As a result, the south was dominated by deep-water, fine-grained deposits derived from source areas in central Hunan and from the Wuyi and Yunkai Massif south of the basin. In contrast, Gu et al. (2015) argued that, by the late stage of the Late Permian (Longtan Formation), the north and south shared a single, basin-wide swamp environment, which favored the formation of coal-bearing sequences [8].

By the Dalong interval of the Late Permian, the HGG Basin began to sink more rapidly. The depression deepened, the sea suddenly spread far inland, and water depths increased quickly. These changes produced alternating deeper troughs and shallower highs, where muddy sediments, silica-rich rocks, and carbonates accumulated. In the southern HGG Basin, deposition was dominated by silica-rich shale and limestone. At the base and top, smaller amounts of calcium-rich shale and limestone containing clastic grains occur. Taken together, the succession records an alternation of deeper and shallower marine conditions. Xu (2012) reached a similar conclusion and argued that, once the southern sector had been infilled and leveled, regional uplift ceased and gave way to slow sinking [9]. This united the southern and northern areas into a continuous swamp, leading to the deposition of the coal-bearing clastic sequence of the Longtan Formation. In summary, during the Late Permian Dalong interval, the region underwent rapid deepening driven by a sudden, large-scale marine flooding and the development of alternating deep and shallow settings.

Pore development in shale is governed mainly by total organic carbon, thermal maturity, the type of organic matter, and the composition of inorganic minerals [10–12]. These organic factors primarily control pores hosted in organic matter [13]. In general, higher organic carbon and greater maturity are associated with more pore space; however, at a low maturity, newly generated liquid hydrocarbons can occupy and block pores, reducing the amount of connected pore space that contributes to flow [14–16]. Beyond organic controls, shales also contain abundant inorganic minerals whose differing physical and chemical properties shape pore networks in different ways [17,18]. Shale is dominated by clay minerals and quartz [19]. The layered crystal structure and interlayers of clays create numerous micropores within and between particles, expanding the available pore space [20,21]. Quartz, being brittle, tends to generate microfractures that enhance permeability [22]. Together, these components exert primary control over the pore volume and fluid flow in shale [23]. Techniques such as mercury intrusion porosimetry (MIP), low-temperature nitrogen adsorption (LTNA), and $CO_2$ adsorption can quantify the microscopic pore structure of shale reservoirs [1]. However, when used together, their results often differ by orders of magnitude, preventing seamless, cross-scale characterization. Moreover, these laboratory methods are largely limited to core analysis and cannot be readily integrated with well logs. As a result, they do not provide a continuous, quantitative downhole evaluation of shale gas reservoir pore structures along the wellbore. To address these gaps, prior studies on coalbed methane reservoirs have compared nuclear magnetic resonance cryoporometry (NMRC) with LTNA [24,25]. NMRC consistently reports larger total pore volumes. This difference arises mainly because (1) NMRC captures a greater fraction of information from poorly connected or nominally closed pores, and (2) LTNA's underlying models have inherent limitations, particularly for pores smaller than ~10 nm and for parts of the meso-to-macropore range. These findings highlight the value of NMRC as a complementary tool for pore structure characterization [24,25].

Based on the above contents, this study, through the combined technology of nuclear magnetic resonance cryoporometry (NMRC) and Image recognition software (Image-J v1.8.0), clarifies the pore size distribution of Permian shale in the HGG Basin. The purpose of this study is to characterize the macroscopic parameters of Permian shale and reveal the level of reservoir space development in Permian shale. The controlling factors of porosity and pore structure are demonstrated. The results of this study will contribute to the large-scale exploration of Permian shale in southern China.

## 2. Geological Setting

The Hunan–Guizhou–Guangxi Basin (HGG Basin) lies in the southern Yangtze Platform and covers more than 80,000 $km^2$ (Figure 1a). During the Early to Middle Permian,

pronounced tectonic extension and volcanism created widespread deep-water depositional conditions across the basin. The stratigraphic record preserves both shallow- and deep-water deposits: shallow-marine carbonate sedimentation formed the Wuchiaping and Changxing formations, whereas deep-water shales, mudstones, and siltstones constitute the Longtan and Dalong formations (Figure 1b). Bivalve, cephalopod, and brachiopod fossils are identifiable in the Dalong Formation.

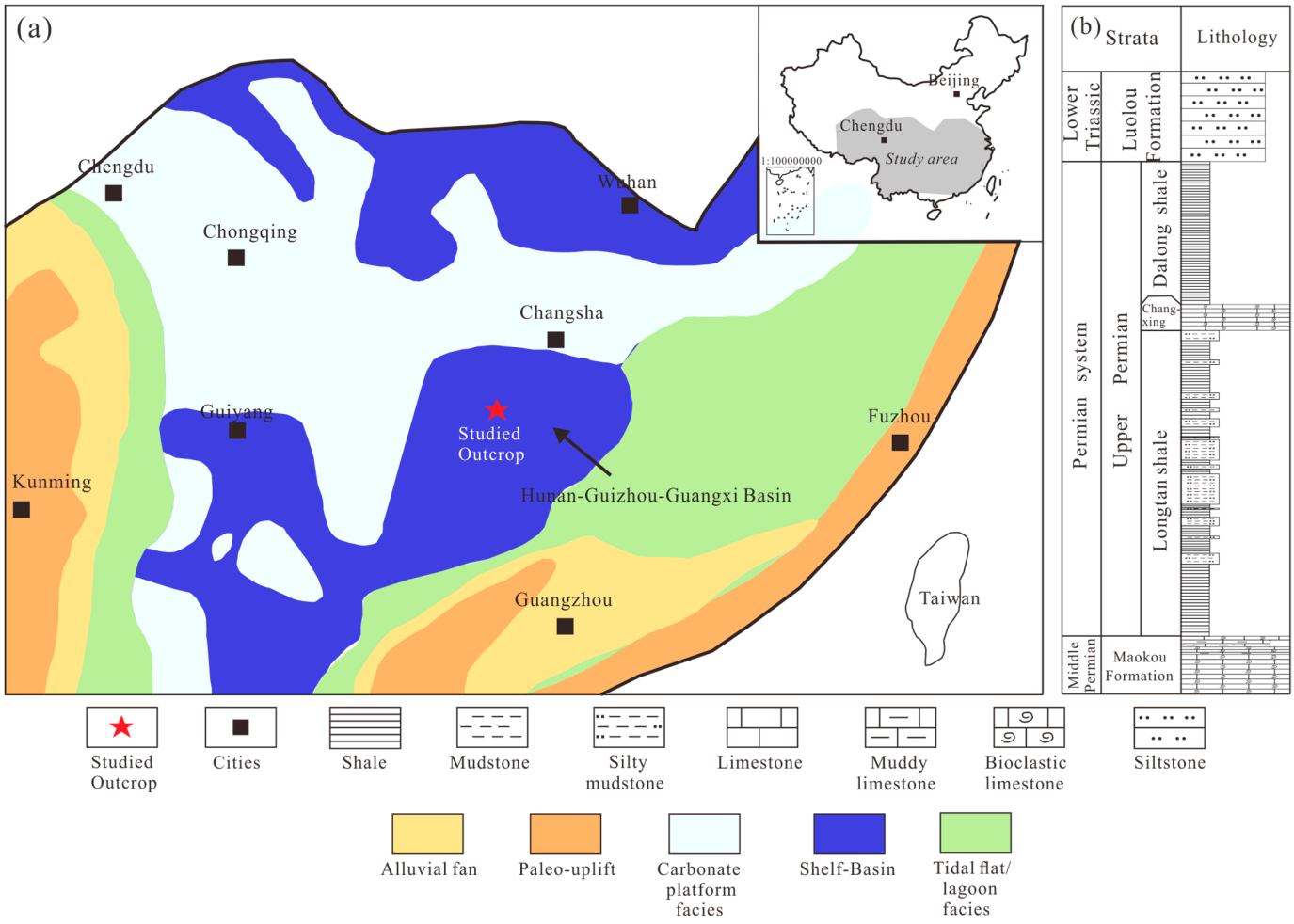



**Figure 1.** (**a**) The sedimentary environment of the Permian shale in Hunan–Guizhou–Guangxi Basin. (**b**) Generalized stratigraphy of Upper Permian in the Hunan–Guizhou–Guangxi Basin.

In the eastern HGG Basin, bivalves are represented by *Aviculopecten* spp. (Figure 2a). Cephalopods are dominated by *Huananoceras* sp., *Pseudogastrioceras* sp., *Huananoceras cf. qianjiangensis (MS)*, *Pseudogastrioceras cf. szichuanensis (MS)*, and *Pseudotirolites cf. asiaticus (Gaevel)* . Brachiopods are mainly *Martima cf. trigueta Gem*. Together, this assemblage indicates deposition on a marine shelf (Figure 2b). By contrast, in the central HGG Basin, the Dalong Formation consists chiefly of thick successions of thin-bedded, dark gray-to-black, silica-rich shale with minor interbeds of clay-rich, fine-grained limestone and chert-bearing limestone (Figure 2c,d). The shale shows abundant horizontal lamination, recording quiet, oxygen-poor bottom waters. Locally, large, wavy lamination is present, likely formed by storm waves or deep-water bottom currents. These lithofacies and sedimentary structures indicate that, during the deposition of the Dalong Formation in the basin center, deep and shallow shelf conditions alternated (Figure 2e,f). The outcrop examined in this study is located in the central HGG Basin (Figure 1a).

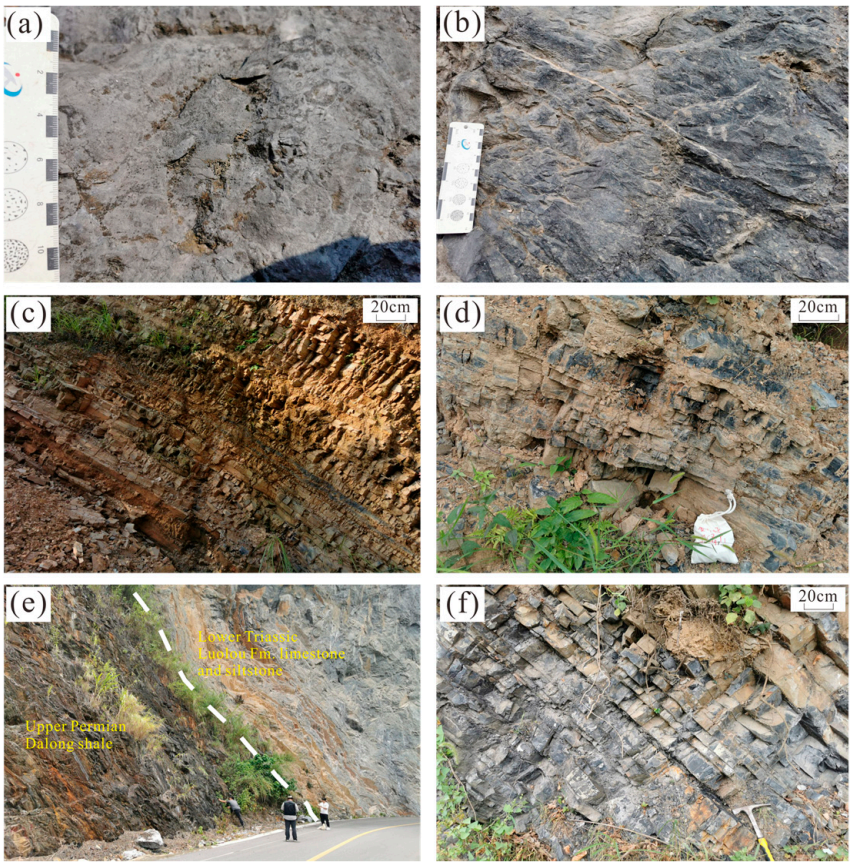



**Figure 2.** Macroscopic characteristics of Permian shale in the studied outcrop of Hunan–Guizhou–Guangxi Basin. (**a**) Gray bioclastic limestone of Changxing Formation.(**b**) Gray limestone of Changxing Formation (**c**) Permian Longtan Fm. shale is characterized by frequent changes in different rock types.(**d**) Organic-rich black shale of Longtan Formation. (**e**) The boundary between the black shale of the Dalong Formation and the overlying Triassic siltstone and limestone. (**f**) Black, organic-rich shale in Dalong Formation.

## 3. Samples and Methods

### *3.1. Sample*

A hundred outcrop shale samples from the studied outcrop in the Central HGG Basin were collected for analyses of total organic carbon (TOC) content and mineral composition. Based on the determination results of mineral compositions, shale facies are classified into multiple types (Table 1). Porosity was determined for 46 of the 100 samples. Pore distribution was determined through nuclear magnetic resonance cryoporometry (NMRC) tests performed on seven cylindrical rock samples (Table 2).

**Table 1.** Classification scheme of Permian shale facies.

| Shale Facies Symbols TOC | High TOC Content | Medium TOC Content | Low TOC Content | Ultra-Low TOC Content |
|---|---|---|---|---|
| Clayey | HM | MM | LM | ULM |
| Siliceous | HS | MS | LS | ULS |
| Carbonate–Siliceous | HCS | MCS | LCS | ULCS |
| Carbonate | HC | MC | LC | ULC |

**Table 2.** NMR fractal dimension calculation results and mineral content of Permian shale in Hunan–Guizhou–Guangxi Basin.

| Strata | Shale Facies | $D_A$ | Correlation Coefficient of $D_A$ | $D_S$ | Correlation Coefficient of $D_S$ | Quartz (%) | Feldspar (%) | Clay Mineral (%) | Illite (%) | Chlorite (%) |
|---|---|---|---|---|---|---|---|---|---|---|
| Dalong | HM | 1.061 | 0.8573 | 2.9888 | 0.7179 | 14.9 | 9.8 | 45.9 | | |
| Dalong | MM | 1.0645 | 0.8563 | 2.9915 | 0.8507 | 16.4 | 13.8 | 58.6 | | |
| Dalong | LM | 1.2236 | 0.8641 | 2.9903 | 0.8554 | 25.3 | 12.6 | 55.4 | 15 | 23 |
| Dalong | MM | 1.1192 | 0.8493 | 2.9906 | 0.8707 | 14.3 | 9.5 | 61.6 | | |
| Longtan | ULCS | 1.1267 | 0.8503 | 2.9844 | 0.8135 | 31.2 | 13.5 | 22.9 | | |
| Longtan | LM | 1.0813 | 0.8549 | 2.9868 | 0.8051 | 12.1 | 13.2 | 51.1 | 27 | 11 |
| Longtan | MCS | 1.1426 | 0.8441 | 2.9902 | 0.8552 | 18.7 | 15 | 35.3 | 30 | 10 |

### *3.2. Experiments*

Mineral composition was determined using X-ray diffraction (XRD). For each shale sample, the clay-sized fraction (<2 μm) was isolated by settling and prepared as oriented slides. Samples were repeatedly rinsed with distilled water, placed in a 2000 mL quartz beaker with 1500 mL distilled water, thoroughly mixed, and left at 25 °C for 20 h. The upper suspension (<2 μm) was pipetted into centrifuge tubes and spun at 2500 rpm for 10 min; the precipitate collected from the tube bottom constituted the <2 μm fraction. The concentrate was resuspended in 2 mL of distilled water, and the slurry was spread onto two flat glass plates (20–30 cm) to form oriented slides. These were air-dried and then treated with ethylene glycol. The ethylene glycol treatment was carried out in vapor, at a set temperature of 600, for approximately 12 h. X-ray diffraction was performed on a Bruker D8 Advance X-ray powder diffractometer (Bruker AXS, Karlsruhe, Germany) with a Cu radiation source (instrument voltage 4.0 kV; tube current 40 mA; scan rate 250/min; step size 0.0167°; 2θ range 3–25°). Mineral surface morphology was examined with an FEI Quanta 250 FEG scanning electron microscope (accelerating voltage 20 kV; working distance 10 mm). All analyses were conducted at the State Key Laboratory of Oil and Gas Reservoir Geology and Exploitation, Southwest Petroleum University.

The Gibbs–Thomson equation serves as a fundamental expression describing the influence of interface curvature on the thermodynamic properties of substances, primarily elucidating the variation patterns in chemical potential induced by surface effects in small-scale particles (such as nuclei or nanoparticles) and their consequential impact on the phase equilibrium; the Gibbs–Thomson effect asserts that the curvature of a material alters its chemical potential, resulting in differences in solubility, melting point, or vapor pressure between small particles and the bulk phase, fundamentally because a reduced curvature radius increases the proportion of surface atoms, thereby significantly enhancing the surface energy contribution and elevating the system's chemical potential. The Gibbs–Thomson equation is presented as follows:

$$\Delta\mu = \frac{2\gamma V_m}{r}$$

In the above equation, $\Delta\mu$ is the chemical potential difference, $\gamma$ is the energy per unit area of the interface, $J/m^2$, $V_m$ is the volume occupied by one mole of substance, $m^3/mol$, and $r$ is the radius of curvature at the interface, m.

The Gibbs–Thomson equation provides the theoretical basis for nuclear magnetic resonance cryoporometry (NMRC). It links the phase-change temperature of a liquid confined in a pore to the pore size. With a suitable probe liquid, monitoring melting or freezing within the pores allows for the determination of the pore size distribution [26]. As temperature rises, the confined probe begins to melt first in micropores with a width below 10 nm, and then in progressively larger pores with a width above 10 nm, increasing the liquid fraction. Under the Gibbs–Thomson relationship, the cumulative increase in liquid volume with temperature mirrors the cumulative pore volume from small to large pores.

Thus, by accurately measuring the liquid volume during a controlled temperature ramp of a porous sample saturated with the probe, one can derive its pore size distribution. For practical use, water and several organic solvents with melting points near room temperature are well suited as NMRC probe liquids.

NMR is well suited for characterizing fluids in pores and monitoring phase changes in porous media. The signal relaxation times of a substance in its solid and liquid states typically differ by several orders of magnitude, allowing NMR to distinguish solid and liquid water and organic solvents. This makes it possible to track only the liquid fraction as temperature varies and, using the Gibbs–Thomson equation, derive the pore size distribution. This study conducted low-temperature NMRC with a Niumag NMRC12-010V system (Niumag, Suzhou, China) that includes gas supply, drying, refrigeration, analysis, and control subsystems. The instrument uses a homogeneous permanent magnet operating at 12.73 MHz, with the field in homogeneity below $3 \times 10^{-5}$ and stabilized at 305.15 ± 0.02 K. The minimum echo time is <48 μs, and the RF coil has a 10 mm probe. The temperature controller provides ±0.02 K accuracy, with a ramp rate of 1 K/min. Samples were loaded into 2.5 mL chromatography vials and placed inside the coil for measurement.

### *3.3. Fractal Dimension Calculation Based on NMR Data*

Fractal geometry provides a framework to quantify irregularity and self-similarity in complex porous media [27,28]. Prior studies show that the pore systems of reservoir rocks exhibit fractal behavior. In three-dimensional Euclidean space, the fractal dimension of pore structures ranges from 2 to 3; values closer to 2 indicate more uniform pores, smoother pore-throat surfaces, and better reservoir quality. Conversely, higher fractal dimensions imply stronger heterogeneity, rougher pore surfaces, and poorer reservoir quality. Building on this principle, this study applies an approximate fractal geometry relationship for the NMR $T_2$ spectrum derived by Zhang et al. [29]. This study estimates the fractal dimension of pore structures in shale samples using piecewise regression. The governing equations are presented in the following section.

$$lgS_V = (3 - D)lgT_2 + (D - 3)lgT_{2max}$$

In the above equation, $T_{2max}$ is the maximum transverse relaxation time, $D$ is the fractal dimension, and $S_V$ is the percentage of the total pore volume, with relaxation times shorter than a specified $T_2$ value. If the shale pore network is self-similar and exhibits fractal behavior, $lgS_V$ is linearly related to $lgT_2$. The coefficients of this regression can then be used to estimate the fractal dimension of the pore structure.

## 4. Results

### *4.1. Macroscopic Characteristics of Permian Shale*

#### 4.1.1. Organic Matter Abundance

Organic geochemical measures of shale are critical for evaluating source rocks in conventional oil and gas and are central to appraising shale gas reservoirs. Data from North American shale gas basins show that a higher organic matter content generally corresponds to a greater gas generation potential [11,12]. Shale gas is also stored by adsorption on organic surfaces; at a given pressure, richer organic content leads to higher amounts of adsorbed gas. To characterize and evaluate shale gas reservoirs, the primary geochemical indicators include total organic carbon (TOC), thermal maturity (Ro), organic matter type (kerogen), hydrocarbon phase, and gas quantity and composition. In this study, we use TOC to represent the abundance of organic matter in shale.

This study measured total organic carbon (TOC) in 141 samples from the Longtan and Dalong formations. Across the outcrop, TOC varies markedly with depth, ranging from 0.24 to 6.36%, with a mean of 1.91% (Figure 3). In the Dalong Formation shales, TOC ranges from 0.58 to 4.36% (mean 2.26%). In the upper Longtan shales, TOC is 0.50 to 2.48% (mean 1.15%). In the lower Longtan shales, TOC is 0.14 to 6.36% (mean 2.18%). Taken together, these data indicate that the lower Longtan shales have the highest organic carbon and the greatest gas generation potential, followed by the Dalong shales; the upper Longtan shales are the lowest. At the facies scale, TOC also varies substantially among shale types. The facies labeled HM (as defined in this study) in the lower Longtan and lower Dalong show the highest TOC, with a mean of 4.1%, followed by the MCS facies in the lower Longtan (mean 3.4%). The MM facies in the lower Longtan averages 3.1% TOC.

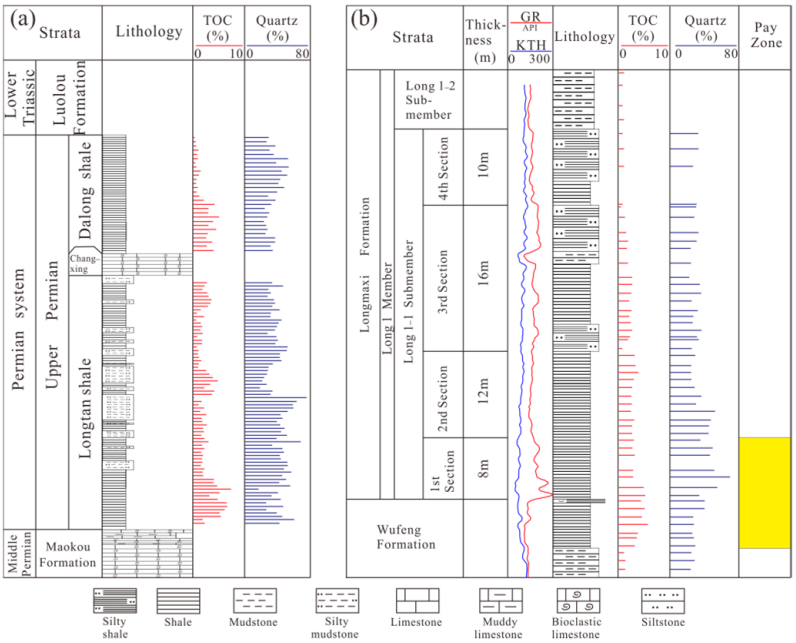



**Figure 3.** Vertical variation in organic matter abundance and quartz content in Permian shale and LMX shale. (**a**) Permian shale in the studied outcrop of Hunan–Guizhou–Guangxi Basin. (**b**) LMX shale in Southern Sichuan Basin.

A comparison with the productive interval of the LMX Formation in the Sichuan Basin shows that the Permian shales have organic carbon contents similar to marine shales. In the favorable interval of the Dalong Formation, the average organic carbon content is comparable to that of the LMX pay zone, whereas the lower part of the Longtan Formation contains even more. These findings indicate that the organic-rich shales in the lower Longtan and Dalong formations in the study area provide a strong basis for hydrocarbon generation and have a high generation potential.

#### 4.1.2. Microscopic Components of Organic Matter

Sapropelic organic matter—primarily amorphous bituminite derived from algal remains—is a dominant constituent of many shale reservoirs (Pickel et al., 2017) [30]. Formed under reducing conditions, this material lacks a fixed shape and sharp boundaries and typically occurs as flocculent to nebulous masses (Khan et al., 2020) [31]. Sapropelic organic matter predominantly consists of long-chain aliphatic hydrocarbons with minor amounts of cycloalkanes and heteroatomic functional groups, characterized by a high hydrogen-to-carbon atomic ratio ($H/C > 1.5$) and low oxygen-to-carbon atomic ratio ($O/C < 0.1$). Following SY/T 5125-2014 (Identification and classification of kerogen macerals by transmitted-light fluorescence), this study used a Leica DM4500 P polarized

fluorescence microscope to identify kerogen macerals in Permian shales [32]. The organic-rich intervals contain abundant bituminite, which commonly fills pores within or lies in contact with authigenic (diagenetically formed) minerals and occurs as irregular bodies (Figure 4).

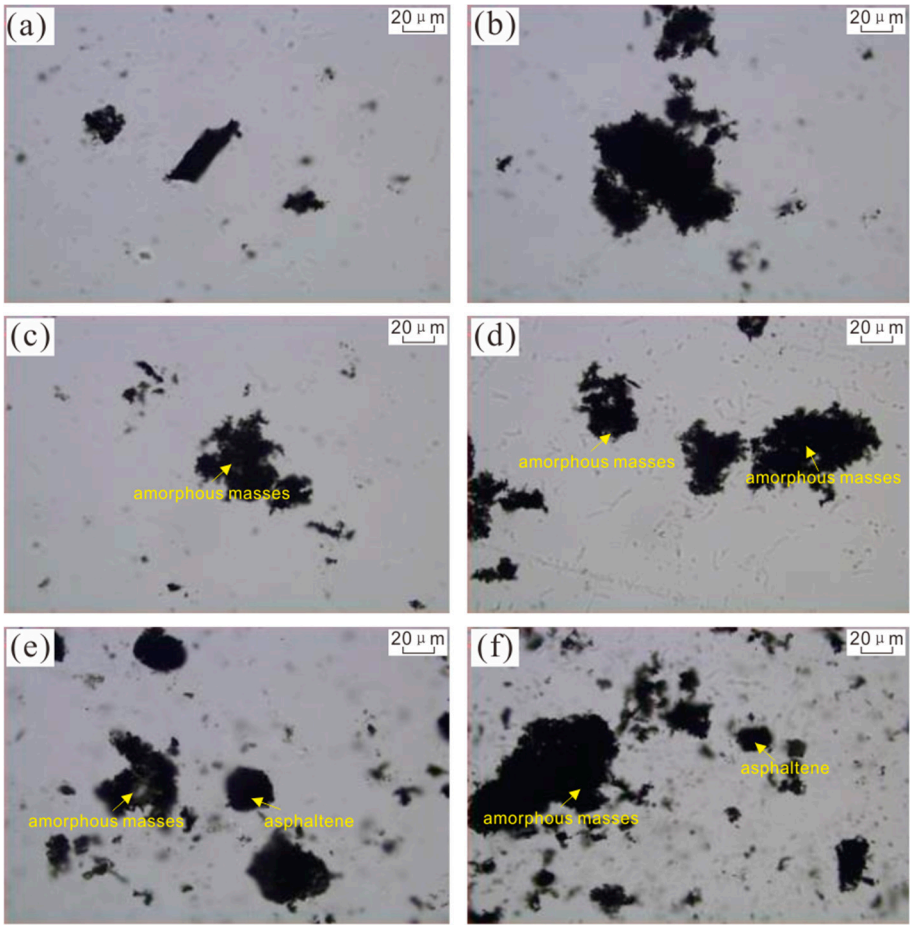



**Figure 4.** Kerogen maceral of organic matter in the Permian shale of Hunan–Guizhou–Guangxi Basin. (**a**) Fraction of solid bitumen in shale of Longtan Formation. (**b**) Asphaltene in shale of Longtan Formation. (**c**) Amorphous masses in shale of Longtan Formation. (**d**) Amorphous masses in shale of Dalong Formation. (**e**) Asphaltene and amorphous masses in shale of Dalong Formation. (**f**) Solid bitumen and fraction of asphaltene in shale of Dalong Formation.

Microscopic identification and counts show that the Permian shales of the HGG Basin are overwhelmingly dominated by algal/lipid-rich organic matter. Across six samples, these components account for 90–96% of the organic matter (mean 93.83%), indicating a predominance of Type I kerogen. For context, the exinite group—plant-derived components from reproductive organs, epidermal tissues, and secretions—can be recognized by distinctive morphologies and is commonly subdivided into sporinite (spores), cutinite (cuticles), and resinite (resins). Sporinite typically appears as circular to oval or flattened ring-like bodies that may deform into worm-like or filamentous shapes under compaction and can occur as small spore aggregates. Cutinite, derived from primary epidermal tissues, is mechanically tough and commonly appears as curved or banded fragments. Resinite, formed from plant resins, gums, waxes, and lipid secretions [33], generally occurs as round to oval bodies with smooth, sharp outlines, flat surfaces, and little internal structure. However, in our kerogen microscopy of the organic-rich Permian shales from the study area, exinite was not observed.

Vitrinite forms chiefly from the gelified tissues of higher plants—stems, leaves, and woody fibers—whereas marine vitrinite is derived mainly from the humified remains of lower marine plants [34]. Vitrinite is primarily composed of aromatic cluster units linked by methylene bridges, ether bonds, or thioether bonds, characterized by moderate hydrogen-to-carbon atomic ratios ($0.8 < H/C < 1.2$) and intermediate oxygen content, reflecting a macromolecular framework centered on condensed aromatic rings. Under scanning electron microscopy (SEM), vitrinite appears dark with sharp boundaries and a dense, uniform, flat surface, occurring as bands or masses of variable width [35]. Within structureless vitrinite, the homogeneous type is most common; it is uniformly dense, and no finer features are visible even at higher magnification. In Permian outcrops of the HGG Basin, abundant higher-plant debris is present and could supply substantial vitrinite to the shale; nevertheless, the microscopic analysis of kerogen from organic-rich shale intervals did not detect vitrinite.

Inertinite consists of microscopic kerogen components formed when plant lignocellulose is converted to a charcoal-like material through charring. These components are chemically stable and largely unreactive, representing the inert fraction of kerogen. The most common type is fusinite, which preserves plant cellular structures particularly well. In scanning electron microscopy, it appears relatively bright; longitudinal sections show a fibrous texture that commonly parallels bedding [33]. In the HGG Basin, Permian outcrop and core samples contain abundant higher-plant debris that could have supplied substantial inertinite to the shale. Nevertheless, the microscopy of kerogen in the organic-rich shale intervals did not identify inertinite.

Solid bitumen is the residue of liquid hydrocarbons generated in a source rock that failed to migrate and were later thermally cracked. It is common in highly overmature shales. Solid bitumen is formed via the radical recombination of polycyclic aromatic clusters, contains virtually no aliphatic chains, and exhibits an extremely low hydrogen-to-carbon atomic ratio ($H/C < 0.5$) and a low oxygen-to-carbon ratio. As noted by Loucks et al. (2007) [36], it typically occurs as very homogeneous bands or compact masses. During the conversion of liquids to gas and solid bitumen, thermal shrinkage causes the material to coalesce into clumps. The interiors show little porosity, or only a few isolated, relatively large pores, generally larger than 100 nm and commonly triangular, spherical, or elliptical. Consistent with this, Cai et al. (2016) and Dong et al. (2015) reported that solid bitumen in the LMX shale (southeastern Chongqing) and North American Horn River Shale contains only a few large pores [37,38]. In the Permian shales of the HGG Basin, microscopic kerogen contains a minor fraction of solid bitumen, about 4–10%.

#### 4.1.3. Organic Matter Maturity

Organic matter maturity refers to the degree of thermal evolution that sedimentary organic matter undergoes during burial, driven primarily by temperature and time over geological scales. Vitrinite reflectance ($V_{Ro}$) is the most reliable indicator of organic matter maturity and is widely used to assess the maturity of source rocks from the Late Paleozoic onward. In the HGG Basin, Permian marine organic-rich shales lack vitrinite derived from higher plants but commonly contain small amounts of solid bitumen, providing a basis for investigating their thermal evolution. Wang et al. (2020), by comparing laboratory thermal simulations with samples from natural maturity series, demonstrated that, when VRo exceeds 1.5%, solid bitumen reflectance closely matches vitrinite reflectance [39]. Thus, in high to overmature shales ($V_{Ro} > 3.50\%$), solid bitumen reflectance can be used as a practical proxy for $V_{Ro}$.

This study analyzed five Permian shale facies samples for reflectance (Figure 5). All measurement points correspond to solid bitumen reflectance. The bitumen reflectance ($B_{Ro}$)

values are uniformly high, averaging 3.85%, indicating a very high thermal maturity; thus, $B_{Ro}$ can be treated as equivalent vitrinite reflectance ($V_{Ro}$). Across stratigraphic intervals, shales in the lower Longtan Formation show distinctly higher reflectance than those in the other units.

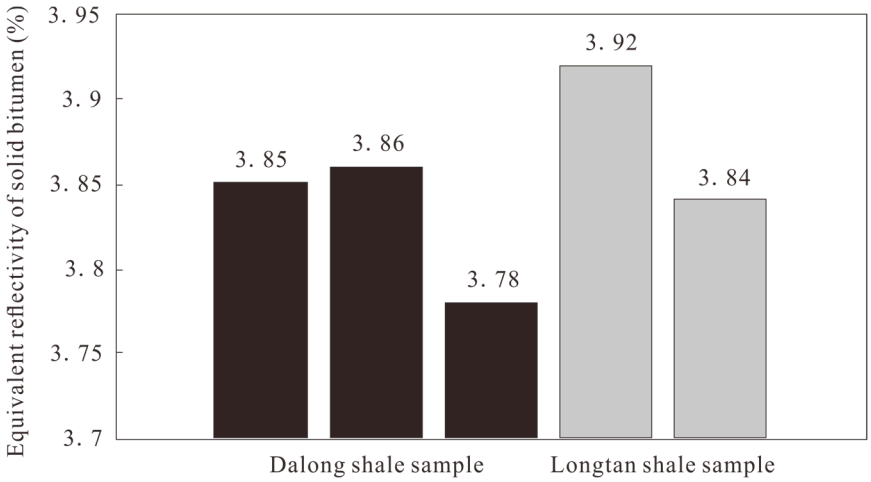



**Figure 5.** Equivalent reflectivity of solid bitumen in the Permian shale of Hunan–Guizhou–Guangxi Basin.

#### 4.1.4. Mineral Composition and Brittleness Index

Shale is a fine-grained sedimentary rock with a complex makeup that includes minerals derived from land, minerals formed in place, and organic matter. The mineral assemblage records the sediment source and governs key reservoir properties—pore and fracture space, gas adsorption, natural fracture development, and the success of hydraulic fracturing—making mineralogy central to shale gas reservoir evaluation. Mineral constituents can be identified through macroscopic observation, light microscopy, electron microscopy, and X-ray diffraction, which together provide a comprehensive view of mineral types and textures. In Permian shales, mineralogy is notably complex: clay minerals, quartz, feldspar, and carbonates are dominant; minor phases include pyrite, siderite, and pyroxene, with occasional small amounts of gypsum and anhydrite. The clay minerals in Permian shales are chiefly illite, chlorite, and mixed-layer illite–smectite, while kaolinite is scarce. These clay mineral characteristics indicate that Permian shales are in the late diagenetic stage.

Siliceous minerals in the Permian shales are dominated by quartz and feldspar. X-ray diffraction shows that siliceous mineral content spans 16.3% to 75.3%, with a mean of 39.5%. In the Dalong Formation, content ranges from 23.8% to 54.0% (mean 35.2%) and is relatively low in the middle and lower intervals. In the Longtan Formation, the upper member contains 27.6% to 52.1% (mean 38.1%), whereas the lower member spans 16.3% to 75.3% (mean 42.6%). Within the lower Longtan, the ULS shale facies has the highest siliceous content (mean 64.2%), followed by the HM facies (mean 40.0%). Compared with the pay zones of the Longmaxi Formation in the HGG Basin, the lower Longtan exhibits siliceous contents similar to marine shales. Higher siliceous contents generally indicate a greater brittleness and better suitability for hydraulic fracturing, which benefits later stimulation. By contrast, the HM shale facies in the lower Dalong Formation has a relatively low siliceous content, which diminishes shale reservoir quality.

Shale suitability for hydraulic fracturing is commonly characterized by the brittleness index (BI), for which multiple evaluation methods exist. In China, current practice largely adapts empirical formulas developed during North American shale gas exploration and production. These approaches quantify brittleness from mineral composition or elastic

parameters and help identify intervals most amenable to hydraulic fracturing. The mineral-based BI can be computed directly from laboratory or log-derived mineralogical data, making it practical for routine evaluation. In the Permian shales, BI shows a gradual decrease vertically (Figure 6). In the lower Longtan Formation, BI ranges from 16.8 to 92.6 with a mean of 52.8; in the upper Longtan Formation, it ranges from 34.7 to 84.4 with a mean of 51.8. In the Dalong Formation, BI ranges from 28.9 to 65.9 with a mean of 43.8. Within the lower Longtan Formation, the ULS subunit has the highest BI (mean 85.0%), followed by the HM subunit (mean 49.0%). In the lower Dalong Formation, the HM subunit is relatively less brittle, with a mean BI of 36.9%. Compared with the pay zone of Longmaxi shale in the Sichuan Basin, the Permian shales generally have a lower BI and therefore exhibit only moderate suitability for hydraulic fracturing (Figure 6).

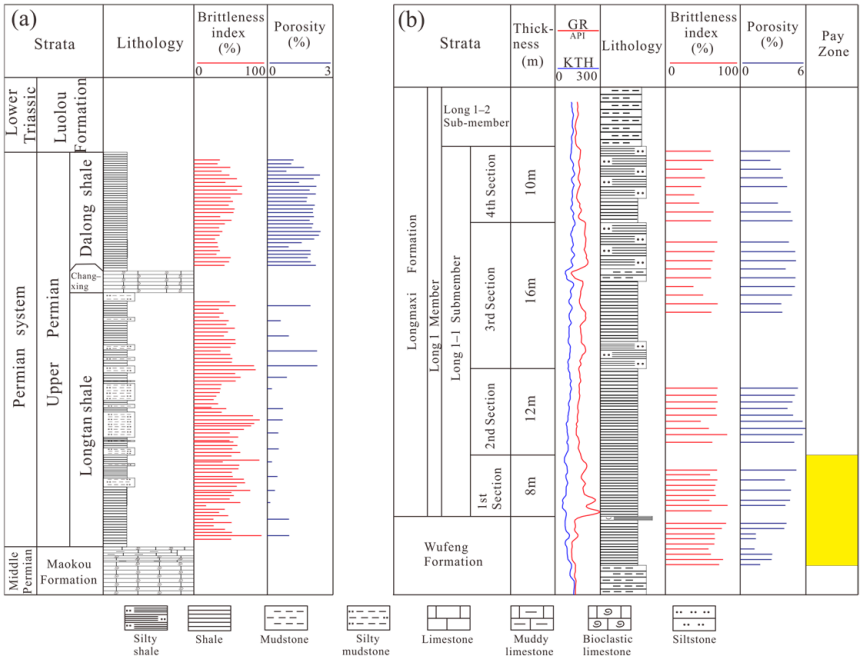



**Figure 6.** Vertical variation in brittleness index and porosity in the Permian shale and LMX shale. (**a**) Permian shale in the studied outcrop of Hunan–Guizhou–Guangxi Basin. (**b**) LMX shale in Southern Sichuan Basin.

### *4.2. Porosity of Permian Shale*

Shale reservoirs must meet certain physical property requirements. Porosity is the main parameter used to estimate the volume of free gas. During production, free gas stored in the rock matrix and fractures is produced first, followed by adsorbed gas. As a distinctive reservoir type, shale is characterized by low porosity. Porosity reflects the degree of pore development, generally increasing with total organic carbon (TOC) and decreasing with burial compaction and higher confining stress where rock or other geological materials experience equal force from all directions due to the weight of overlying material. Several techniques are used to measure shale porosity, including nuclear magnetic resonance (NMR), liquid saturation, and the Boyle's law dual-chamber method; however, the results from different methods are often not directly comparable [40]. In this study, we used NMR to determine total porosity and to analyze the samples' rock property characteristics. Based on these NMR measurements, porosity varies markedly in the Permian shales. In the lower Longtan Formation, porosity ranges from 0.11% to 1.01% (mean 0.52%). In the upper Longtan Formation, porosity ranges from 0.17% to 2.26% (mean 1.22%). In the Dalong Formation, porosity ranges from 0.83% to 2.38%. Compared with the marine Longmaxi pay zone in the Sichuan Basin, Permian shale porosity is generally lower (Figure 6).

### *4.3. Microscopic Pore Structure*

#### 4.3.1. Microfracture Types and Microscopic Characteristics

Interlayer bedding is a type of fissure that develops along layers under the influence of sedimentation, generally representing strong hydrodynamic conditions (Figure 7a,b). Interlayer bedding can be seen to develop within the clayey shale facies of the Dalong Formation, generally filled entirely with calcite (Figure 7c,d).

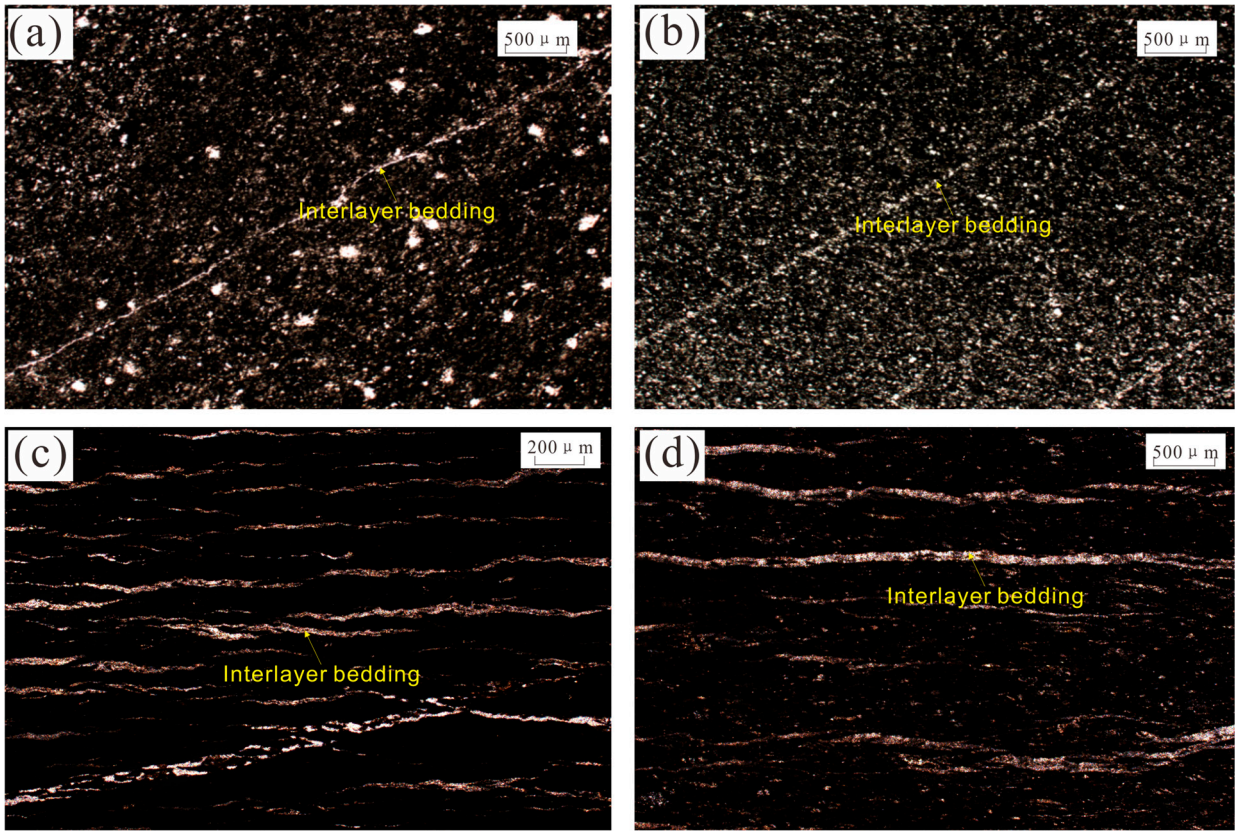



**Figure 7.** Interlayer bedding in the Permian shale of Hunan–Guizhou–Guangxi Basin. (**a**) Interlayer bedding in clayey shale of Dalong Formation. (**b**) Interlayer bedding in siliceous shale of Dalong Formation. (**c**) Interlayer bedding in laminated clayey shale of Dalong Formation. (**d**) Interlayer bedding in laminated clayey shale of Dalong Formation.

Burial-related shrinkage microfractures are typically irregular and discontinuous (Figure 8a). They form early after deposition as changes in temperature and pressure drive physical and chemical reactions within the shale, and they are not associated with tectonic stress or deformation (Figure 8b). These cracks are visible under an electron microscope, tend to develop along contacts between softer and harder minerals, and occur throughout all layers of the Permian shale (Figure 8c).

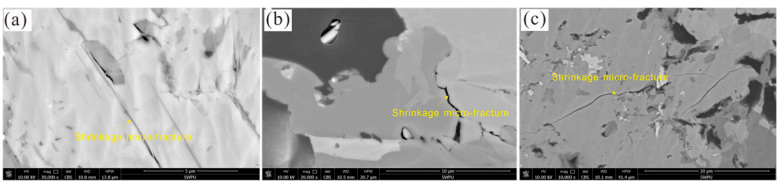



**Figure 8.** Shrinkage micro-fracture in the Permian shale of Hunan–Guizhou–Guangxi Basin. (**a**) Shrinkage micro-fracture in illite of shale in Longtan Formation. (**b**) Shrinkage micro-fracture between illite and chlorite of shale in Dalong Formation. (**c**) Shrinkage micro-fracture in illite of shale in Dalong Formation.

4.3.2. Pore Types and Microscopic Characteristics

Organic matter pores (OMPs) are widely recognized as a key component of the shale gas pore system. Although OMPs often appear as isolated voids in two-dimensional sections, three-dimensional observations reveal good connectivity. In two dimensions, common morphologies include irregular, bubble-like, elliptical to subrounded, and honeycomb-like shapes. OMP abundance varies widely among shale facies, but pore shapes are broadly similar—typically bubble-like and nearly round (Figure 9a). In the lower Longtan Formation, the MCS facies shows sparse OMPs; most are elliptical, 50–150 nm in diameter (Figure 9b). In the upper Longtan Formation, the LM facies has better organic pore development; pores are elliptical to near-round, about 100–500 nm (Figure 9c). The strongest development occurs in the lower Longtan Formation and in the Dalong Formation HM and MM facies, where bubble-like OMPs commonly form chains; diameters reach up to 1100 nm (Figure 9d).

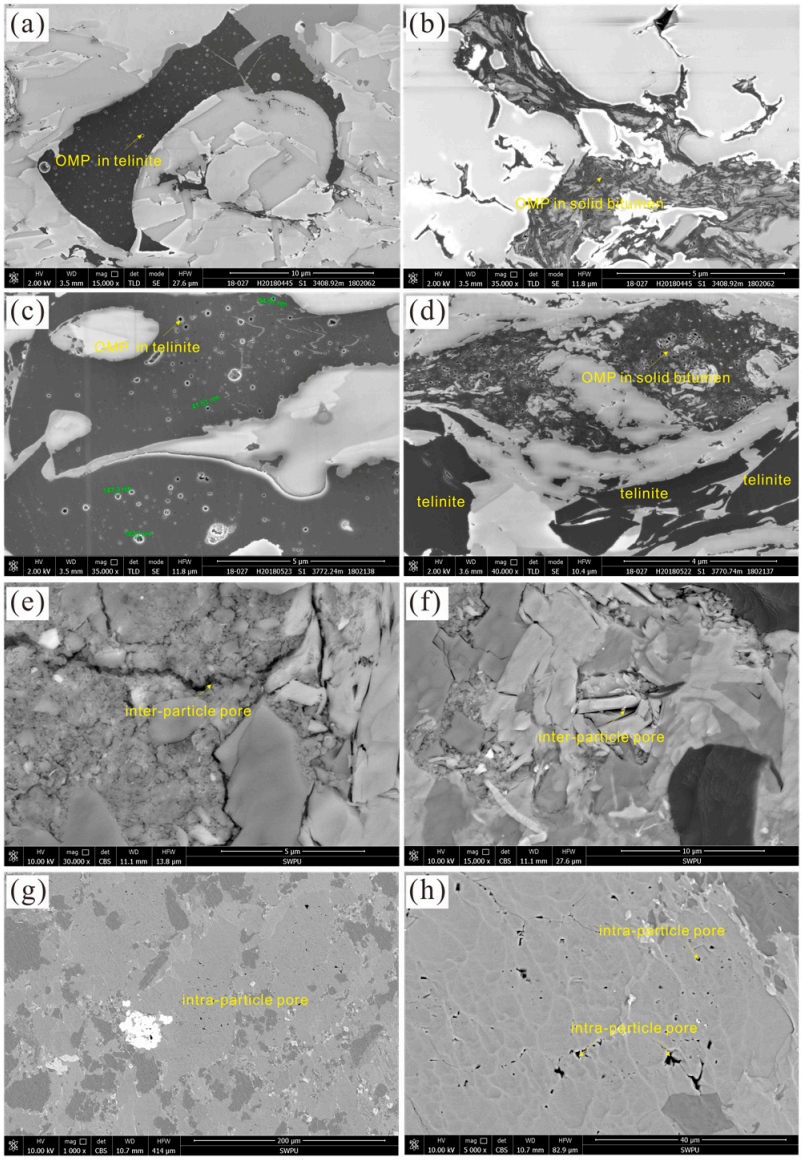



**Figure 9.** Pore types and microscopic characteristics in the Permian shale of Hunan–Guizhou–Guangxi Basin. (**a**) OMP in telinite. (**b**) OMP in solid bitumen. (**c**) OMP in telinite. (**d**) OMPs are observed in solid bitumen. (**e**) Inter-particle pore is observed between different particles. (**f**) Inter-particle pore is observed between different particles. (**g**) Intra-particle pore in calcite. (**h**) Intra-particle pore in calcite.

Inter-particle pores in shale occur between ductile and brittle grains. Ductile grains are largely clay aggregates, pellets, and organic matter, whereas brittle grains are mostly quartz, feldspar, pyrite formed in place, and biological fragments. In shallow burial, these pores are common and well connected, creating an effective pore network. With increasing depth, rising pressure and temperature promote compaction and cementation, which progressively reduce inter-particle pores. Ductile grains deform under compaction and can choke pore openings, weakening connectivity. In contrast, the dissolution of unstable minerals may locally create or enlarge inter-particle pores.

Inter-particle pores are present across all Permian shale types. They occur mainly between hard mineral grains, at contacts between hard and soft particles, and along the edges of hard grains. Where less stable minerals such as calcite and feldspar meet more stable minerals, localized dissolution creates pores (Figure 9e). Inter-particle pores also form at contacts between organic matter and clay, driven by heating of the organic matter or dehydration of the clay (Figure 9f). Intra-particle pores are chiefly voids within grains; pores within individual crystals also occur locally. Most formed during diagenesis, with a smaller proportion of primary origin. The main types include moldic pores produced by partial or complete dissolution, pores between fossil fragments, intercrystalline pores in framboidal (raspberry-like) pyrite, cleavage-plane and intragranular pores inside clay and mica grains, and pores within spherical carbonate grains and pellets (ooids and peloids) (Figure 9g). In Permian shales, intragranular porosity is dominated by interlayer spaces within clay minerals, intercrystalline pores in framboidal pyrite, cavities within biological remains, and pores inside calcite and feldspar grains. In calcite, feldspar, and dolomite, these intra-particle pores commonly occur as triangular, angular, or elongated dissolution voids and microfractures (Figure 9h).

This study combined field-emission scanning electron microscopy with Image-J image analysis to classify pore types directly from images and to quantify their proportions across Permian shale facies (Figure 10). The proportions of pore types differ markedly among facies. The Dalong Formation HM facies and the lower Longtan Formation MCS facies closely resemble marine shale, being dominated by organic matter pores (OMPs) (Figure 10). In these two facies, OMPs account for 67% and 66%, respectively. OMPs are next most abundant in the Dalong Formation LM facies and the upper Longtan Formation ULM facies, at 55% and 41%. Microfractures are relatively well developed in the lower Longtan Formation MM facies, accounting for 19%. In that facies, organic matter pores are less common, comprising 22%.

### *4.4. Pore Size Distribution Based on NMRC*

NMRC pore size distribution curves indicate that HM in the Dalong Formation has the highest microporosity (Figure 11). OMPs in this facies are well developed, with micropore volumes reaching up to 0.12 $cm^3/g$. By comparison, MM and MCS in the Longtan Formation have a higher proportion of macropores (Figure 11), but much smaller mesopore and micropore volumes (averaging about 0.02 $cm^3/g$). Consequently, their OMPs are less developed than those in the Dalong Formation. In particular, MM in the lower Longtan interval exhibits elevated macropore volumes, indicating well-developed macropores and/or microfractures (Figure 11).

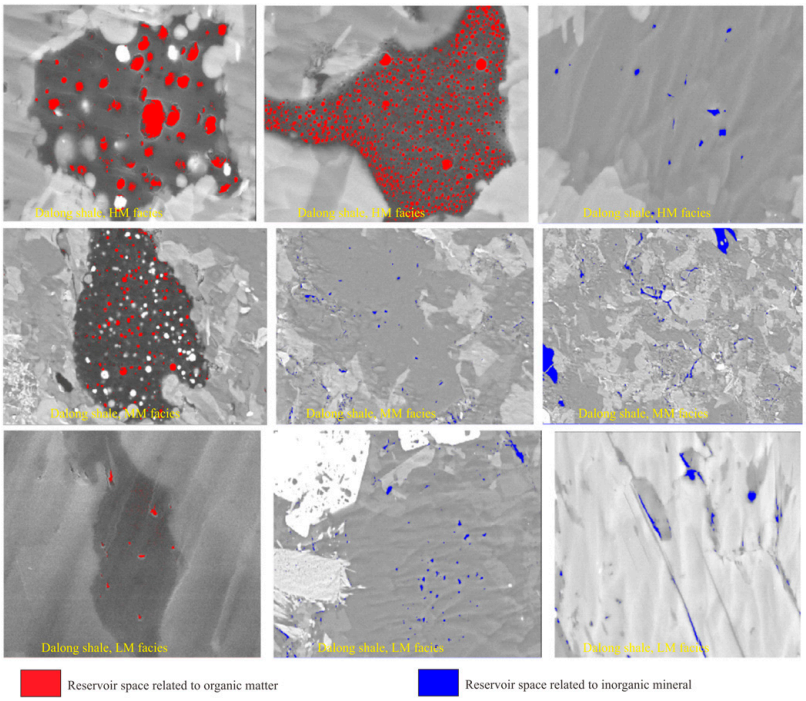



**Figure 10.** Image-J Software processing results in the Permian shale of Hunan–Guizhou–Guangxi Basin.

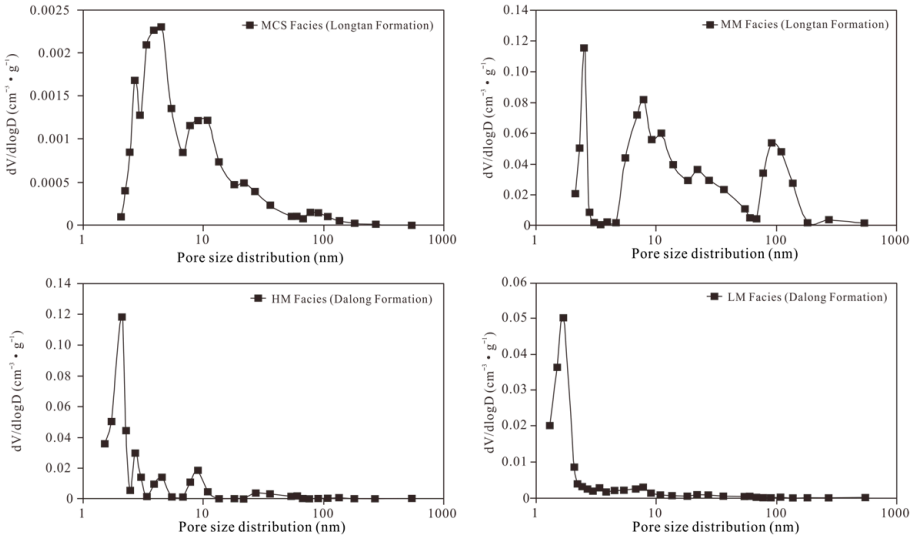



**Figure 11.** Pore size distribution of the Permian shale in Hunan–Guizhou–Guangxi Basin based on NMRC.

### *4.5. Fractal Characteristics of Pore Structure*

Figure 12 shows the log–log plot of $lgT_2$ versus $lgS_V$ for all samples. The slopes of the fitted lines on either side of the shale data differ markedly. Guided by centrifuge calibration, we used the mean cutoff relaxation time ($T_{2c}$) as the threshold, dividing the data into two ranges: $T_2 < 0.5$ ms and $T_2 \geq 0.5$ ms. We then performed separate linear regressions for the two ranges and calculated the fractal dimensions of adsorption pores ($D_A$) and flow pores ($D_S$). The results are summarized in Table 1.

The calculated $D_A$ and $D_S$ indicate that the Permian shale exhibits distinctly different fractal characteristics on the two sides of $T_2 = 0.5$ ms. Accordingly, we partitioned the pore system into two regimes and, for each, evaluated how the fractal dimensions of adsorption and flow pores relate to brittle mineral content.

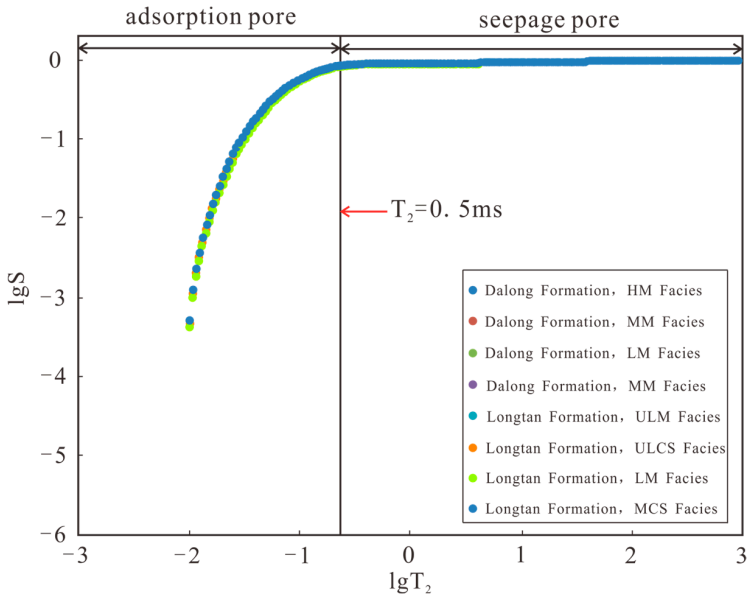



**Figure 12.** Cross-plot of $T_2$ vs. $S_V$ in the Permian shale of Hunan–Guizhou–Guangxi Basin.

## 5. Discussions

### *5.1. Analysis of the Controlling Factors of Porosity*

Shale reservoirs have varied mineral compositions and abundant organic matter. This diversity gives rise to many pore types and a complex set of controls. Pores hosted within organic matter, in particular, govern how the pore network develops and thereby affect the reservoir's physical properties. In the lower Longtan Formation and the Dalong Formation, porosity shows a clear positive correlation with TOC and a negative correlation with clay content. By contrast, in the upper Longtan Formation, porosity is not correlated with TOC but is positively correlated with clay content (Figure 13). These patterns indicate that TOC is the primary control on porosity in the lower Longtan and Dalong formations, whereas clay minerals dominate control in the upper Longtan. Scanning electron microscopy of argon-ion-polished samples shows that, aside from a few organic pores, the upper Longtan shales contain abundant pores between grains and between layers within clay minerals (Figure 9), which account for most of the porosity. In the lower Longtan and Dalong formations, organic pores are pervasive, explaining the difference in the dominant controls on porosity between these intervals.

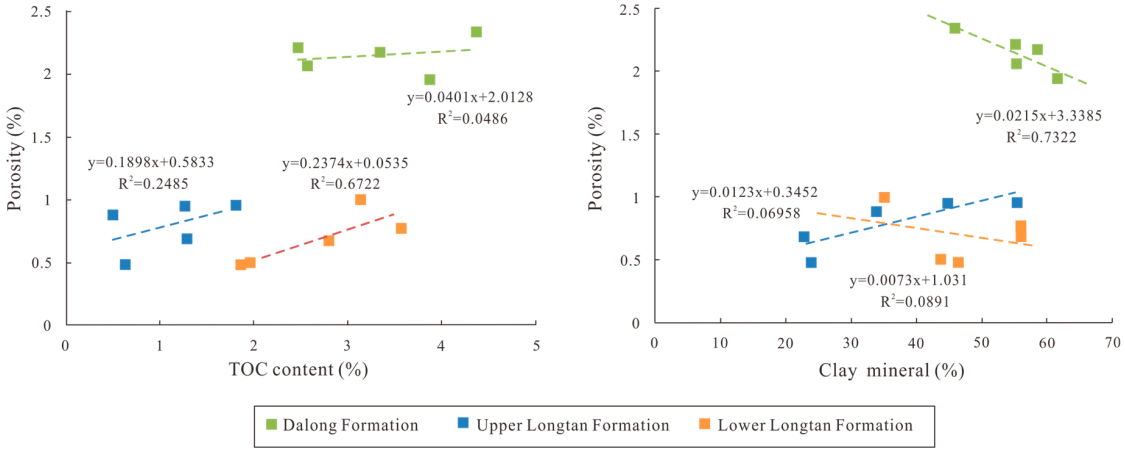



**Figure 13.** Cross-plot of porosity vs. TOC and clay minerals in the Permian shale of Hunan–Guizhou–Guangxi Basin.

### *5.2. Analysis of the Controlling Factors of Pore Structure*

The analysis shows that, in Permian shale samples, the fractal dimension of adsorption pores has a weak positive correlation with quartz content ($R^2$ = 0.332) and no clear relationship with feldspar ($R^2$ = 0.015). In contrast, the fractal dimension of flow pores has a weak negative correlation with quartz ($R^2$ = 0.2579) and likewise shows no clear relationship with feldspar ($R^2$ = 0.2074). This pattern arises because, across most sections of the Permian shale, pores associated with organic matter are the main source of small pores. As a result, variations in quartz and feldspar have little influence on the development of adsorption pores. At larger scales, however, higher proportions of brittle minerals reduce the irregularity and heterogeneity of flow pores, leading to lower fractal dimensions (Figure 14).

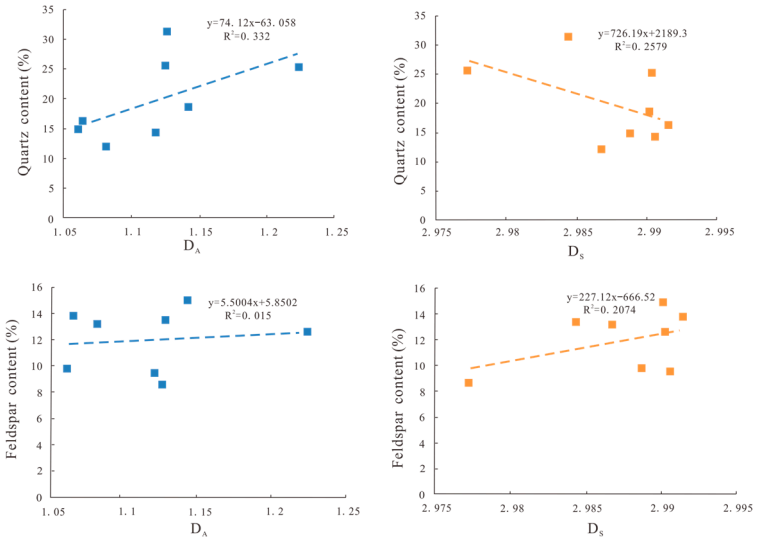



**Figure 14.** Cross-plot of brittle mineral content vs. fractal dimension in the Permian shale of Hunan–Guizhou–Guangxi Basin.

Clay minerals are a key control on the development of Permian shale reservoirs. Their adsorption capacity decreases in the order: montmorillonite, illite–smectite mixed layer, kaolinite, chlorite, and illite. The XRD results show that kaolinite is nearly absent in the study area. We therefore compare the fractal dimensions of adsorption-related and flow-related pores with total clay, illite, and chlorite contents (Figure 14).

The results show that the fractal dimension of adsorption pores ($D_A$) has no clear relationship with the total clay content, is negatively correlated with the illite content, and shows no clear relationship with the chlorite content. In contrast, the fractal dimension of flow pores ($D_S$) shows a weak positive correlation with the total clay content, a clear positive correlation with the illite content, and a negative correlation with the chlorite content (Figure 15). These patterns reflect differences in mineral–fluid interactions. When illite interacts with water, it tends to break down and plug pores, an effect that is especially pronounced in the smallest pores hosted by organic matter; this accounts for the negative correlation between $D_A$ and illite. In larger, flow-bearing pores, disintegrated illite roughens otherwise smooth walls between and within grains, increasing structural complexity and raising $D_S$. By contrast, reactions between chlorite and pore fluids tend to smooth the walls of flow pores, reducing structural complexity and lowering $D_S$.

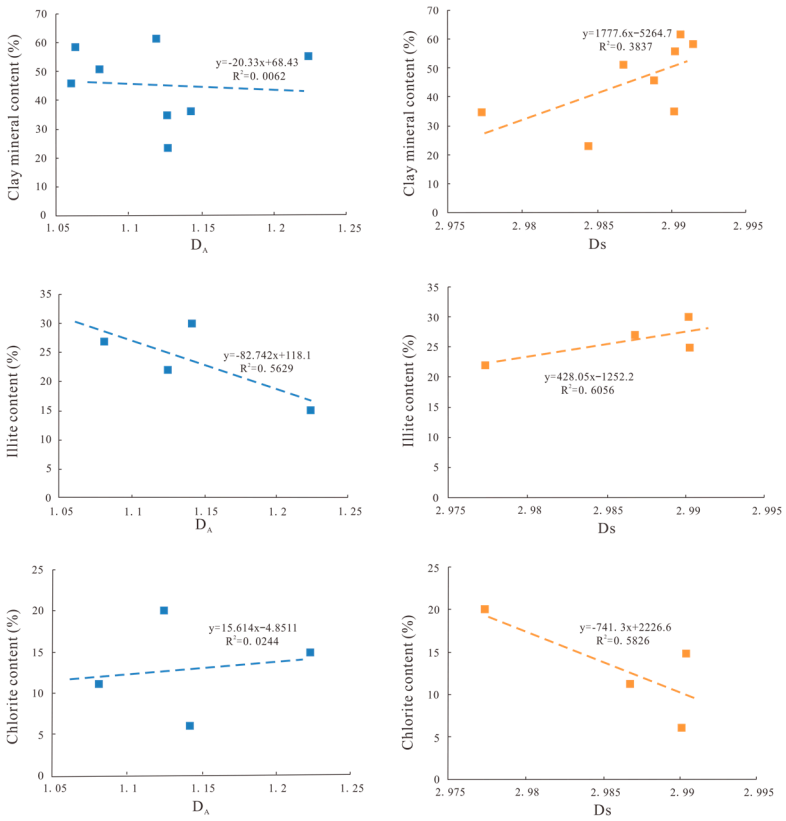



**Figure 15.** Cross-plot of clay mineral content vs. fractal dimension in the Permian shale of Hunan–Guizhou–Guangxi Basin.

### *5.3. Geological Implication*

In shale reservoirs, natural gas primarily exists in free and adsorbed states, with the fractal dimension serving as a critical indicator of heterogeneity in porous media, encompassing surface roughness and pore structure. Higher fractal dimensions signify more complex pore structures that impede gas percolation and diffusion while enhancing storage capacity. Specifically, elevated $D_A$ values correlate with rougher pore surfaces, increased adsorption sites, and hindered gas diffusion, whereas increased $D_S$ values reflect greater pore space complexity, heightened pore connectivity tortuosity, and diminished flow capacity, collectively resulting in reservoirs with high fractal dimensions exhibiting weakened inherent gas flow but strengthened adsorption potential. Analysis integrating large-field SEM pore observations and gas content data reveals that siliceous shale develops intricate 3D pore–fracture networks, where high TOC fosters abundant organic-hosted pores, larger mesopore volumes and specific surface areas enhance free gas storage for scalable extraction, and brittle mineral dominance facilitates complex fracture networks post-hydraulic fracturing. Conclusively, the Permian shale in the study area demonstrates distinct multi-scale fractal characteristics correlating with reservoir parameters, enabling a comprehensive evaluation of premium intervals through the integrated assessment of shale quality indices and fractal dimension attributes.

## 6. Conclusions

(1) In the Dalong Formation shales, TOC ranges from 0.58 to 4.36% (mean 2.26%). In the upper Longtan shales, TOC is 0.50 to 2.48% (mean 1.15%). In the lower Longtan shales, TOC is 0.14 to 6.36% (mean 2.18%). The lower Longtan shales have the highest organic carbon and the greatest gas generation potential, followed by the Dalong shales; the upper Longtan shales are the lowest. The Permian shales in the HGG Basin have organic carbon

contents similar to marine shales. In the favorable interval of the Dalong Formation, the average organic carbon content is comparable to that of the Longmaxi pay zone, whereas the lower part of the Longtan Formation contains even more. These findings indicate that the organic-rich shales in the lower Longtan and Dalong formations in the study area provide a strong basis for hydrocarbon generation and have a high generation potential.

(2) In the lower Longtan Formation and the Dalong Formation, porosity shows a clear positive correlation with TOC and a negative correlation with clay content. In the upper Longtan Formation, porosity is not correlated with TOC but is positively correlated with clay content. TOC is the primary control on porosity in the lower Longtan and Dalong formations, whereas clay minerals dominate the control in the upper Longtan. The upper Longtan shales contain abundant pores between grains and between layers within clay minerals, which account for most of the porosity. In the lower Longtan and Dalong formations, organic pores are pervasive, explaining the difference in the dominant controls on porosity between these intervals.

(3) Clay minerals are a key control on the development of Permian shale reservoirs. The fractal dimension of adsorption pores ($D_A$) has no clear relationship with total clay content, is negatively correlated with illite content, and shows no clear relationship with chlorite content. In contrast, the fractal dimension of flow pores ($D_S$) shows a weak positive correlation with total clay content, a clear positive correlation with illite content, and a negative correlation with chlorite content. When illite interacts with water, it tends to break down and plug pores, an effect that is especially pronounced in the smallest pores hosted by organic matter; this accounts for the negative correlation between $D_A$ and illite. In larger, flow-bearing pores, disintegrated illite roughens otherwise smooth walls between and within grains, increasing structural complexity and raising $D_S$. By contrast, reactions between chlorite and pore fluids tend to smooth the walls of flow pores, reducing structural complexity and lowering $D_S$.

**Author Contributions:** Conceptualization, Y.S. and Y.J.; methodology, M.L.; validation, X.W.; formal analysis, J.H.; investigation, Y.G. and Y.S.; data curation, Y.J.; writing—original draft preparation, Y.S. and Y.J.; writing—review and editing, X.W. and M.L.; visualization, J.H.; supervision, Y.G. and X.W.; project administration, J.H. and M.L. All authors have read and agreed to the published version of the manuscript.

**Funding:** This research was supported by the National Natural Science Foundation of China. (No.: 42272171) and the National Natural Science Foundation of China (No. 42302166).

**Institutional Review Board Statement:** Not applicable.

**Informed Consent Statement:** Not applicable.

**Data Availability Statement:** Data are contained within the article.

**Conflicts of Interest:** Authors Xiangfeng Wei and Jingyu Hao were employed by the Sinopec Exploration Company. The remaining authors declare that the research was conducted in the absence of any commercial or financial relationships that could be construed as a potential conflict of interest.

## References

1. Gu, Y.F.; Cai, G.Y.; Hu, D.F.; Wei, Z.H.; Liu, R.B.; Han, J.; Fan, Z.W.; Hao, J.Y.; Jiang, Y.Q. Geochemical and Geological Characterization of Upper Permian Linghao Formation Shale in Nanpanjiang Basin, SW China. *Front. Earth Sci.* **2022**, *10*, 883146. [CrossRef]
2. Gu, Y.F.; Hu, D.F.; Wei, Z.H.; Liu, R.B.; Hao, J.Y.; Han, J.; Fan, Z.W.; Jiang, Y.Q.; Wang, Y.S.; Xu, Q.D. Sedimentology and Geochemistry of the Upper Permian Linghao Formation Marine Shale, Central Nanpanjiang Basin, SW China. *Front. Earth Sci.* **2022**, *10*, 914426. [CrossRef]

3. Zhang, H.Q.; Cao, J.F.; Lan, B.F.; Chen, Y.; Zhang, Q.; Men, Y.P.; Feng, X.T.; Yu, Q. Organic matter enrichment model of Permian Capitanian-Changhsingian black shale in the intra-platform basin of Nanpanjiang basin. *Front. Earth Sci.* **2024**, *12*, 1403575. [CrossRef]
4. Wang, M.; Yu, X.N.; Liu, S.; Cheng, Y.L.; Guo, J.J.; Wang, Z.L.; Duan, X.M. Sedimentary Paleo-Environment and Reservoir Heterogeneity of Shale Revealed by Fractal Analysis in the Inter-Platform Basin: A Case Study of Permian Shale from Outcrop of Nanpanjiang Basin. *Fractal Fract.* **2025**, *9*, 795. [CrossRef]
5. Yin, H.F.; Jiang, H.S.; Xia, W.C.; Feng, Q.L.; Zhang, N.; Shen, J. The end-Permian regression in South China and its implication on mass extinction. *Earth-Sci. Rev.* **2014**, *137*, 19–33. [CrossRef]
6. Wang, M.K.; He, X.P.; Xu, Y.P.; Jin, W. Geological characteristics of shale gas in Dalong Formation of Well Xiangye 1 in Lianyuan sag, Xiangzhong depression. *China Pet. Explor.* **2021**, *26*, 86–98.
7. Liu, Z.H. Sedimentary facies differentiation and its mechanism during Permian in Central Southern Hunan. *Chin. J. Geol.* **2005**, *40*, 510–517.
8. Gu, Z.X.; Peng, Y.M.; He, Y.B.; Hu, Z.Q.; Zhai, Y.J. Geological conditions of Permian sea-land transitional facies shale gas in the Xiangzhong depression. *Geol. China* **2015**, *42*, 288–299.
9. Xu, Y.G. The Sedimentary Facies and Favourable Area Forecast of the Marine Shale Formations in Xiangzhong Area. Master's Thesis, Chengdu University of Technology, Chengdu, China, 2012.
10. Ross, D.J.K.; Bustin, R.M. The importance of shale composition and pore structure upon gas storage potential of shale gas reservoirs. *Mar. Pet. Geol.* **2009**, *26*, 916–927. [CrossRef]
11. Slatt, R.M.; O'Brien, N.R. Pore types in the Barnett and Woodford gas shales: Contribution to understanding gas storage and migration pathways in fine-grained rocks. *AAPG Bull.* **2011**, *95*, 2017–2030. [CrossRef]
12. Klaver, J.; Desbois, G.; Urai, J.L.; Littke, R. BIB-SEM study of the pore space morphology in early mature Posidonia Shale from the Hils area, Germany. *Int. J. Coal Geol.* **2012**, *103*, 12–25. [CrossRef]
13. Chalmers, G.R.; Bustin, R.M.; Power, I.M. Characterization of gas shale pore systems by porosimetry, pycnometry, surface area, and field emission scanning electron microscopy/transmission electron microscopy image analyses: Examples from the Barnett, Woodford, Haynesville, Marcellus, and Doig units. *AAPG Bull.* **2012**, *96*, 1099–1119. [CrossRef]
14. Anovitz, L.M.; Cole, D.R. Characterization and Analysis of Porosity and Pore Structures. *Rev. Mineral. Geochem.* **2015**, *80*, 61–164. [CrossRef]
15. Milliken, K.L.; Olson, J.E.; Rudnicki, M.; Awwiller, D.N.; Pigott, J.D. Organic matter-hosted pore system in the Marcellus Formation (Devonian), Pennsylvania. *AAPG Bull.* **2013**, *97*, 177–200. [CrossRef]
16. Klaver, J.; Urai, J.L.; Littke, R.; Krooss, B.M. BIB-SEM pore characterization of mature and post-mature gas shales. *Int. J. Coal Geol.* **2016**, *158*, 78–89. [CrossRef]
17. Ko, L.T.; Ruppel, S.C.; Loucks, R.G.; Hackley, P.C.; Zhang, T.; Shao, D. Pore-types and pore-network evolution in Upper Devonian-Lower Mississippian Woodford and Mississippian Barnett mudstones: Insights from laboratory thermal maturation and organic petrology. *Int. J. Coal Geol.* **2018**, *190*, 3–28. [CrossRef]
18. Kala, S.; Turlapati, V.Y.; Devaraju, J.; Rasheed, M.A.; Sivaranjanee, N.; Ravi, A. Impact of sedimentary environment on pore parameters of thermally mature Permian shale: A study from Kommugudem Formation of Krishna Godavari Basin, India. *Mar. Pet. Geol.* **2021**, *132*, 105236. [CrossRef]
19. Bahadur, J.; Chandra, D.; Das, A.; Vishal, V.; Agrawal, A.K.; Sen, D. Pore anisotropy in shale and its dependence on thermal maturity and organic carbon content: A scanning SAXS study. *Int. J. Coal Geol.* **2023**, *273*, 104268. [CrossRef]
20. Ko, L.T.; Loucks, R.G.; Rowe, H.; Adriaens, R.; Sivil, J.E.; Mertens, G. Mudstone diagenesis with depth and thermal maturity in the Cenomanian–Turonian Eagle Ford group. PART II: Diagenetic processes and paragenetic sequence. *Mar. Pet. Geol.* **2024**, *170*, 107085. [CrossRef]
21. Curtis, M.E.; Cardott, B.J.; Sondergeld, C.H.; Rai, C.S. Development of organic porosity in the Woodford Shale with increasing thermal maturity. *Int. J. Coal Geol.* **2012**, *103*, 26–31. [CrossRef]
22. Loucks, R.G.; Reed, R.M.; Ruppel, S.C.; Hammes, U. Spectrum of pore types and networks in mudrocks and a descriptive classification for matrix-related mudrock pores. *AAPG Bull.* **2012**, *96*, 1071–1098. [CrossRef]
23. Wood, J.M.; Sanei, H.; Haeri-Ardakani, O.; Curtis, M.E.; Akai, T.; Currie, C. Solid bitumen in the Montney Formation: Diagnostic petrographic characteristics and significance for hydrocarbon migration. *Int. J. Coal Geol.* **2018**, *198*, 48–62. [CrossRef]
24. Jackson, C.; McKenna, G.B. The melting behavior of organic materials confined in porous solids. *J. Chem. Phys.* **1990**, *93*, 9002–9011. [CrossRef]
25. Guo, W.; Yao, Y.B.; Liu, D.M.; Sun, X.X.; Gao, Y.W. Research on measurement of pores in coals with NMRC technique. *Oil Gas Geol.* **2016**, *37*, 141–148.
26. Galenko, P. *Phase Field Theory of Material Physics*; Springer: Cham, Switzerland, 2024.
27. Gould, D.J.; Vadakkan, T.J.; Poché, R.A.; Dickinson, M.E. Multifractal and Lacunarity Analysis of Microvascular Morphology and Remodeling. *Microcirculation* **2011**, *18*, 136–151. [CrossRef]

28. Lopes, R.; Betrouni, N. Fractal and multifractal analysis: A review. *Med. Image Anal.* **2009**, *13*, 634–649. [CrossRef]
29. Zhang, C.M.; Chen, Z.B.; Zhang, Z.S.; Li, J.; Linhu, S.; Sun, B.D. Fractal Characteristics of Reservoir Rock Pore Structure Based on NMR $T_2$ Distribution. *J. Oil Gas Technol.* **2007**, *29*, 80–86.
30. Pickel, W.; Kus, J.; Flores, D.; Kalaitzidis, S.; Christanis, K.; Cardott, B.J.; Misz-Kennan, M.; Rodrigues, S.; Hentschel, A.; Hamor-Vido, M.; et al. Classification of liptinite–ICCP System 1994. *Int. J. Coal Geol.* **2017**, *169*, 40–61.
31. Khan, I.; Zhong, N.; Luo, Q.; Ai, J.; Yao, L.; Luo, P. Maceral composition and origin of organic matter input in Neoproterozoic–Lower Cambrian organic-rich shales of Salt Range Formation, upper Indus Basin, Pakistan. *Int. J. Coal Geol.* **2020**, *217*, 103319.
32. *SY/T 5125-2014*; Method for Identification Microscopically the Macerals of Kerogen and Indivision of the Kerogen Type by Transmitted-Light and Fluorescence. China National Petroleum Corporation: Beijing, China, 2014.
33. Jiao, S.J.; Zhang, H.; Xue, D.C.; Huang, Z.L.; Liu, G.H. Morphological structure and identify method of organic macerals of shale with SEM. *J. Chin. Electron Microsc. Soc.* **2018**, *37*, 137–144.
34. Zeng, F.G.; Tuo, J.C.; Li, Y.; Cai, C.F. Aromatic Biomar ker Composition Characteristics of Three Kinds of Tertiary Brown Coals in Guangxi. *Aca. Sci. Nat. Univ. Pekin.* **1998**, *34*, 793–800.
35. Jiao, S.J.; Zhang, H.; Xue, D.C. SEM study on organic macerals of shale in Lucaogou Formation Santanghu Basin. *J. Chin. Electron Microsc. Soc.* **2019**, *38*, 257–263.
36. Loucks, R.G.; Ruppel, S.C. Mississippian Barnett Shale: Lithofacies and depositional setting of a deep-water shale-gas succession in the Fort Worth Basin, Texas. *AAPG Bull.* **2007**, *91*, 579–601.
37. Cai, X.; Wang, L.; Jin, Y.X.; Gao, Y.Q.; Cao, H.H.; Ding, A.X. Types and characteristics of organic pore in shale gas reservoir of southeastern Chongqing area. *Nat. Gas Geosci.* **2016**, *27*, 513–519.
38. Dong, T.; Harris, N.B.; Ayranci, K.; Twemlow, C.E.; Nassichuk, B.R. Porosity characteristics of the Devonian Horn River shale, Canada: Insights from lithofacies classification and shale composition. *Int. J. Coal Geol.* **2015**, *141*, 74–90. [CrossRef]
39. Wang, Y.; Qiu, N.S.; Ma, Z.L.; Ning, C.X.; Zheng, L.J.; Zhou, Y.Y.; Fang, G.J.; Rui, X.Q.; Rao, D. Evaluation of equivalent relationship between vitrinite reflectance and solid bitumen reflectance. *J. China Univ. Min. Technol.* **2020**, *49*, 563–575.
40. Li, X.; Liu, P.; Luo, Y.Y.; Fang, C.Q.; Li, B.; Wu, D. Analysis of influencing factors on porosity measurement of shale gas reservoir core. *Prog. Geophys.* **2015**, *30*, 2181–2187.


**Disclaimer/Publisher's Note:** The statements, opinions and data contained in all publications are solely those of the individual author(s) and contributor(s) and not of MDPI and/or the editor(s). MDPI and/or the editor(s) disclaim responsibility for any injury to people or property resulting from any ideas, methods, instructions or products referred to in the content.